Journal of Alloys and Compounds 509 (2011) 10167–10171

Contents lists available at ScienceDirect

Journal of Alloys and Compounds

journal homepage: www.elsevier.com/locate/jallcom

Preparation, structure and photoluminescence of nanoscaled-Nd: $Lu_3Al_5O_{12}$

Lihua Ding[a,b], Qingli Zhang[a,*], Jianqiao Luo[a], Wenpeng Liu[a], Wenlong Zhou[a,b], Shaotang Yin[a]

[a] Anhui Provincial Key Lab of Optical Devices and Materials, Anhui Institute of Optics and Fine Mechanics, Chinese Academy of Sciences, Hefei 230031, China
[b] Graduate School of Chinese Academy of Sciences, Beijing 100039, China

ARTICLE INFO

Article history:
Received 4 February 2010
Received in revised form
27 September 2010
Accepted 28 September 2010
Available online 28 July 2011

Keywords:
Nd:$Lu_3Al_5O_{12}$
Co-precipitation preparation
Structure
Absorption spectrum
Photoluminescence
Lifetime

ABSTRACT

Nd:$Lu_3Al_5O_{12}$ (Nd:LuAG) nano-crystalline was synthesized by co-precipitation method. Its phase transformation, structure, absorption and photoluminescence properties were studied. The Nd:LuAG polycrystalline phase is formed above 900 °C and its particle sizes are in the range of 18–36 nm. The structure of Nd:LuAG was refined by Rietveld method. The lattice parameters and the distortion of Lu^{3+}–O^{2-} polyhedron in Nd:LuAG are larger than that of in pure LuAG. Because the distortion of Lu^{3+}–O^{2-} polyhedron is larger than that of Y^{3+}–O^{2-} polyhedron in YAG and the distance of Lu^{3+}–O^{2-} is smaller than that of Y^{3+}–O^{2-} in YAG, Nd^{3+} in LuAG experiences a stronger crystal field effect, which is proved by the crystal field strength and the chemical environment parameter. The absorption spectrum shows that Nd:LuAG has a broad absorption band at 808 nm with FWHM above 6 nm, which is favorable for improving laser efficiency. The fluorescence lifetime from $^4F_{3/2} \rightarrow {}^4I_{11/2}$ transition is 320 μs and longer than that of Nd:YAG. The longer lifetime is propitious to energy storage. The emission cross section at 1064 nm is 2.89×10^{-19} cm^2, taking into account the Boltzmann distribution of the excited state. The emission cross section in Nd:LuAG is also larger than that of Nd:YAG, which is useful for laser operation. All results indicate that Nd:LuAG is a promising crystal material to apply in high energy lasers.

1. Introduction

Rare-earth ions doped garnet single crystals have been widely used for optical application [1–4]. Nd^{3+} doped yttrium aluminum garnet (Nd:YAG) is one of the most-known solid state laser materials. When the crystallography sites of Y^{3+} in YAG are substituted by Lu^{3+}, another garnet compound $Lu_3Al_5O_{12}$ (LuAG) is formed. LuAG has gained much attention due to its similar properties to YAG [5–7]. Compared with YAG, LuAG has higher hardness and density. In addition, LuAG also has high thermal conductivity (9.6 W/mK) [8]. These physical properties make it a very good luminescent host. For example, Pr, Yb and Ce doped LuAG crystals have attracted a lot of attention for high power lasers and scintillator applications [9–11].

A. A. Kaminskii has studied Nd:LuAG luminescence and energy level [12]. It has smaller splitting of $^4F_{3/2}$ state (67 cm^{-1}) than that of Nd:YAG (84 cm^{-1}), which can produce a higher amplification at 1064 nm lasing wavelength. In addition, the Stark energy splitting of $^4I_{9/2}$ reaches about 878 cm^{-1} which is larger than that of Nd:YAG (848 cm^{-1}), indicating that Nd^{3+} experiences a quite stronger crystal field interaction in LuAG than that of in YAG. However, few studies on the difference of crystal field interaction between Nd:LuAG and Nd:YAG were carried out. Hence, here we study this problem from the point of structure, which is helpful to understand the relationship between luminescent mechanism of Nd^{3+} and structure. In addition, the room temperature diffuse reflection absorption and fluorescence spectra of Nd:LuAG were also studied.

2. Experimental

2.1. Sample preparation

The nanoscaled polycrystalline of LuAG has been successfully synthesized by co-precipitin method [13,14], so in this work the nano-crystalline Nd:LuAG was synthesized by this method. Nd_2O_3 (99.999%), Lu_2O_3 (99.999%), $Al(NO_3)_3{\cdot}9H_2O$ (analytical purity), HNO_3 (analytical purity) and $NH_3{\cdot}H_2O$ (analytical purity) were used as the starting materials. The stoichiometric Nd_2O_3 and Lu_2O_3 powders were separately dissolved in the diluent HNO_3 solution (5 mol/L), and the stoichiometric aluminum nitrate ($Al(NO_3)_3{\cdot}9H_2O$) was dissolved in deionized water (the molar ratio of $Lu(NO_3)_3$:$Al(NO_3)_3$:$Nd(NO_3)_3$ = 2.91:5:0.09). After the three solutions were mixed completely, the mixed nitrate solution and aqueous ammonia were dropped simultaneously into ammonia with adequate stir, and the pH value was kept in the range of 7–9. After that, the precipitate was washed with deionized water for several times to remove NH_4^+, NO_3^- and OH^-, and was dried at 110 °C for 32 h, The precursors were ground and calcined at different temperatures (700, 800, 900, 1000, 1100 and 1250 °C) for 5 h, and used as different measurement sample.

2.2. Structure and spectrum measurement

Thermal weight analysis (TG) and differential thermal analysis (DTA) of the precursor were performed on a DT-50 thermal analysis system in air atmosphere with a heating rate of 10 °C/min. The powder structure was characterized by the X-ray

* Corresponding author. Tel.: +86 551 5591039; fax: +86 551 5591039.
E-mail address: zql@aiofm.ac.cn (Q. Zhang).

0925-8388/$ – see front matter © 2011 Published by Elsevier B.V.
doi:10.1016/j.jallcom.2011.07.083

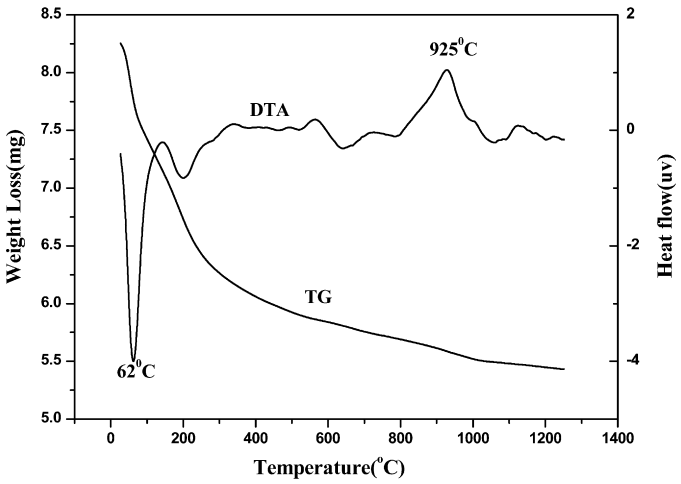

Fig. 1. TG and DTA curves of the precursor of Nd:LuAG powder from 25 °C to 1250 °C.

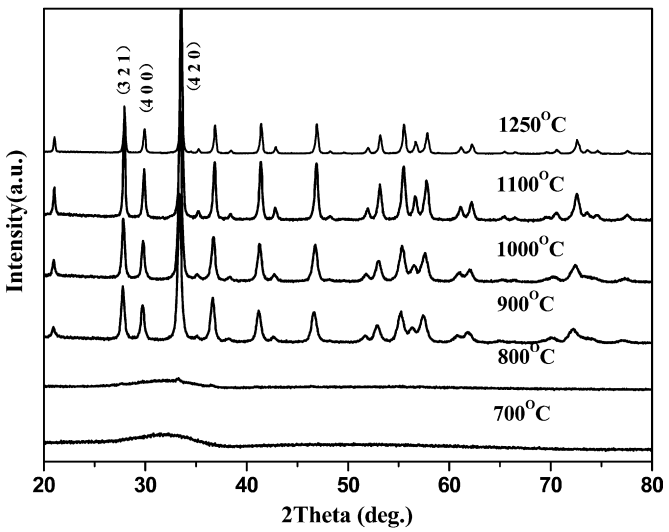

Fig. 2. XRD patterns of the precursor of Nd:LuAG calcined at 700–1250 °C for 5 h.

Table 1
The FWHM of (3 2 1), (4 0 0) and (4 2 0) diffraction peaks and particle sizes of the samples calcined at 900, 1000, 1100 and 1250 °C.

Sample (°C)	(3 2 1) (°)	(4 0 0) (°)	(4 2 0) (°)	Particle size (nm)
900	0.43	0.51	0.43	18
1000	0.36	0.4	0.39	21
1100	0.25	0.3	0.27	30
1250	0.21	0.27	0.21	36

diffraction (XRD), the XRD data were collected by a Philips X'pert Pro X-ray diffractometer using Cu Kα_1 radiation in the 2θ rang of 20–80° with a step size 0.033492° and a count time of 10.16 s per step. The crystal structure was refined by Rietveld method with GSAS 2000 software package [15]. A France Jobin Yvon Fluorolog 3 Tau Fluorescence Spectrophotometer was employed to measure the photoluminescence and fluorescent lifetime, and a Japan Shimadzu Solid Spec-3700 DUV UV-visible-near infrared spectrophotometer was used to measure diffuse reflection absorption spectrum. All measurements were performed at room temperature.

3. Results and discussion

3.1. The thermal transformation of precursor

TG and DTA curves of the precursor of Nd:LuAG are shown in Fig. 1. The TG curve demonstrates that most of the weight loss occurred below 790 °C due to the removal of molecular water and the decomposition of the hydrates. Two major peaks are identified in the DTA curve. The endothermic peak at 62 °C is assigned to the removal of molecular water. The exothermic peak at 925 °C is caused by the crystallization of Nd:LuAG. Fig. 2 shows the XRD patterns of Nd:LuAG precursors calcined at 700, 800, 900, 1000, 1100 and 1250 °C for 5 h. The sample is still amorphous at 800 °C, which demonstrates that Nd:LuAG cannot be synthesized below 800 °C. The XRD patterns of the sample calcined at 900, 1000, 1100 and 1250 °C are consistent with that of pure LuAG (JCPDS 73-1368 [16]) but only with small peak shifts, which indicate that the precursor can transform into Nd:LuAG polycrystalline phase above 900 °C. In the DTA curve in Fig. 1, the crystallization temperature of Nd:LuAG is appreciably higher than the actual phase transition temperature, which may be attributed to the temperature-hysteresis effect of the differential thermal analysis. The DTA result is in good agreement with the XRD result.

The particle size of polycrystalline material can be calculated by Debye Scherrer formula ($d = 0.89\lambda/B\cos\theta$) [17], where d is particle diameter, λ the X-ray wavelength ($\lambda = 1.5406$ Å), B the full width at half maximum (FWHM) of the diffraction peaks, θ diffraction angle. Table 1 shows the FWHM of (3 2 1), (4 0 0) and (4 2 0) diffraction peaks and the particle size of the samples calcined at 900, 1000, 1100 and 1250 °C, respectively. With the increase of calcination temperature, the FWHM decreases and particle size increases, namely, the crystallization degree of the material increases. The average crystalline particle sizes of the samples are less than 50 nm.

3.2. Structure refinement and crystal field effect of Nd:LuAG

According to the above results, the Nd:LuAG powder calcined at 1250 °C has the similar structure to LuAG (garnet structure and cubic system with space group Ia-3d). In LuAG crystal structure, Lu^{3+} occupies Wyckoff site 24c and the site symmetry is D_2. Al^{3+} occupies two sites and the Wyckoff sites are 24d and 16a, respectively. The point symmetry at the Wyckoff site 24d is S_4 and the symmetry at the Wyckoff site 16a is S_6. Dopant Nd^{3+} would replace the site of Lu^{3+}. The coordinates of Lu^{3+}/Nd^{3+} and Al^{3+} are constant, so the only coordinates of oxygen ions at the Wyckoff site of 96 h need to be determined. In addition, the ionic radius of Nd^{3+} (1.00 Å) is larger than that of Lu^{3+} (0.85 Å), which leads to the increase of the lattice length and cell volume of Nd:LuAG.

In order to study the structure changes of LuAG caused by the Nd^{3+} doping, the structure of Nd:LuAG is refined by Rietveld method. The refined curves of Nd:LuAG is shown in Fig. 3. The calculated XRD pattern matches the experimental very well. In Table 2, the refined results of the lattice parameters, cell volume, oxygen atomic coordinates, R_p and R_{wp} are listed. This table shows that the deviation of lattice parameter is 0.0297 Å and the deviation of oxygen atomic coordinates (X, Y, Z) is 0.00092, −0.00354 and −0.00585, respectively. Lattice parameters and cell volume of

Table 2
The lattice parameters and the oxygen atomic coordinates obtained by Rietveld refinement.

Sample	Lattice (Å)	Volume (Å^3)	Oxygen atomic coordinates			R_p	R_{wp}
			X	Y	Z		
Nd:LuAG	11.9361	1700.5	−0.02852	0.05021	0.14511	0.069	0.0974
LuAG [16]	11.9064	1687.7	−0.02944	0.05375	0.15096	0.046	–

Table 3
The bond length and bond angle of Nd:LuAG, LuAG and YAG.

		Nd:LuAG	LuAG	YAG
Bond length (Å)	$Al^{3+}{}_{(1)}$–O^{2-}	1.8640	1.9388	1.9265
	$Al^{3+}{}_{(2)}$–O^{2-}	1.8037	1.7597	1.7682
	Lu^{3+}(Y)–$O^{2-}{}_{(1)}$	2.2987	2.2760	2.3114
	Lu^{3+}(Y)–$O^{2-}{}_{(2)}$	2.4208	2.3832	2.4113
Bond angle (°)	$Al^{3+}{}_{(1)}$–$O^{2-}{}_{(1)}$–Lu^{3+}(Y)	106.066	104.000	104.475
	$Al^{3+}{}_{(1)}$–$O^{2-}{}_{(2)}$–Lu^{3+}(Y)	101.477	100.193	99.848
	$Al^{3+}{}_{(2)}$–$O^{2-}{}_{(1)}$–Lu^{3+}(Y)	92.538	94.173	93.892

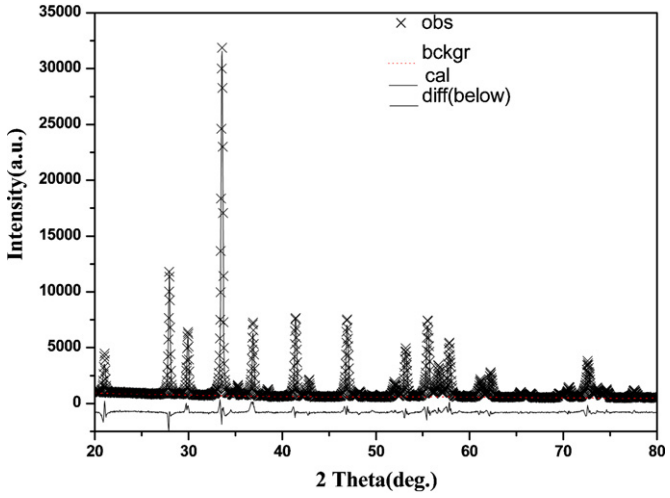

Fig. 3. Rietveld results of Nd:LuAG polycrystalline powder. The experimental data and the calculated are shown by crosses and solid curves, respectively; the bottom curve corresponds to the difference between the experimental and calculated values, and the dot curve is background.

Nd:LuAG are larger than that of LuAG because the smaller Lu^{3+} is partly substituted by the larger Nd^{3+}.

When some Lu^{3+} in LuAG is replaced by Nd^{3+}, the bond length and bond angle would change due to the different ionic radii between Lu^{3+} and Nd^{3+}. In Fig. 4, the structures of Nd:LuAG and LuAG are shown. The values of bond length and bond angle in Nd:LuAG and LuAG are listed in Table 3, respectively. For comparison, the bond length and bond angle of YAG are also listed in Table 3. There are two crystallographic sites of Al^{3+}, labeled site $Al^{3+}{}_{(1)}$ (Wyckoff site 16a) and site $Al^{3+}{}_{(2)}$ (Wyckoff site 24d), which are coordinated with 6 and 4 oxygen atoms, respectively. For Nd:LuAG, the O^{2-} near the four coordinated Lu^{3+} are labeled by $O^{2-}{}_{(1)}$, and the remaining O^{2-} are $O^{2-}{}_{(2)}$.

Compared with LuAG, the $Al^{3+}{}_{(2)}$-O^{2-} bond lengths increase and the $Al^{3+}{}_{(1)}$–O^{2-} bond lengths decrease in Nd:LuAG. Lu^{3+}-$O^{2-}{}_{(1)}$ and Lu^{3+}–$O^{2-}{}_{(2)}$ bond lengths both increase, but the degree of increase of Lu^{3+}–$O^{2-}{}_{(2)}$ is more than that of Lu^{3+}–$O^{2-}{}_{(1)}$, indicating that the Lu^{3+}–O^{2-} polyhedron is enlarged along the b crystallographic axis and the polyhedron is distorted in Nd:LuAG. In addition, in Nd:LuAG the rate of increase of $Al^{3+}{}_{(1)}$–$O^{2-}{}_{(1)}$–Lu^{3+} angle is more than that of $Al^{3+}{}_{(1)}$–$O^{2-}{}_{(2)}$–Lu^{3+}, which indicates that the distances between $O^{2-}{}_{(1)}$ and Lu^{3+} decrease and the distances between $O^{2-}{}_{(2)}$and Lu^{3+} increase. The angles of $Al^{3+}{}_{(2)}$–$O^{2-}{}_{(1)}$–Lu^{3+} are smaller than those of LuAG.

Compared with YAG, the bond length of Lu^{3+}–O^{2-} in LuAG is smaller than that of Y^{3+}–O^{2-}. According to the bond valence of theory, the bond strength is inversely proportional to the bond length, so the Lu^{3+}–O^{2-} bond is stronger than Y^{3+}–O^{2-}. In addition, the length ratio of Lu^{3+}–$O^{2-}{}_{(2)}$ to Lu^{3+}–$O^{2-}{}_{(1)}$ is more than that of Y^{3+}–$O^{2-}{}_{(2)}$ to Y^{3+}–$O^{2-}{}_{(1)}$, which indicated that the distortion degree of Lu^{3+}–O^{2-} polyhedron is more than that of Y^{3+}–O^{2-} polyhedron. The more distorted, the stronger crystal field effect. The strength of crystal field effect can be expressed by $V_{CF} = \sum_{k,q} B_q^k C_q^{(k)}$, where the crystal field parameters B_k^q characterize the interaction between ligands and the central ion, and $C_q^{(k)}$ is the operator of angular part. The crystal field parameters B_k^q of Nd:LuAG and Nd:YAG [18] are listed in Table 4.

The crystal field strength parameter, N_v which can be used to predict the maximum Stark splitting ΔE_{max}, is defined by:

$$N_v = \left[\sum_{k,q} \left(\frac{4\pi}{2k+1} \right) \left| B_q^k \right|^2 \right]^{1/2} \quad (1)$$

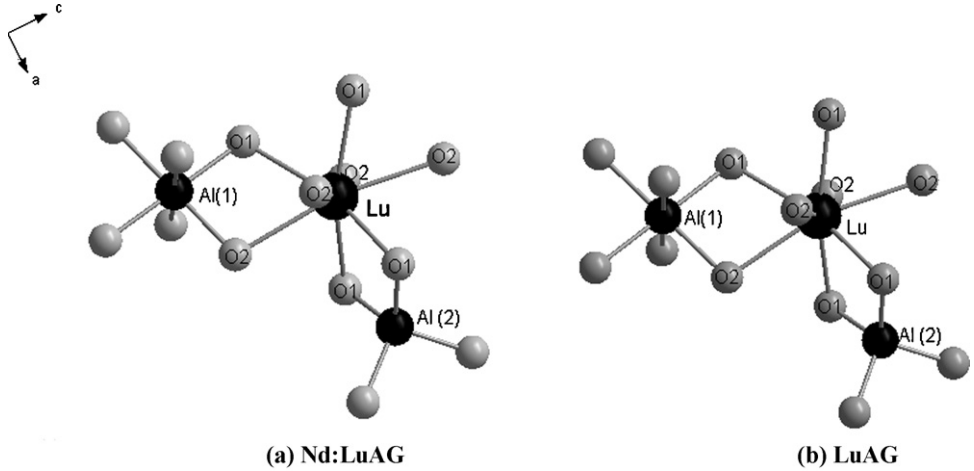

Fig. 4. The structure of (a) Nd:LuAG and (b) LuAG (//b, and b is vertical to paper).

Table 4
The crystal field parameters B_k^q of Nd:LuAG and Nd:YAG (cm^{-1}).

	B_0^2	B_2^2	B_0^4	B_2^4	B_4^4	B_0^6	B_2^6	B_4^6	B_6^6
Nd:LuAG	−280	202	−2881	276	1248	1049	−337	1675	−120
Nd:YAG	−336	209	−2870	414	1159	994	−339	1610	−133

The maximum Stark splitting ΔE_{max} can be written out in the following way:

$$\Delta E_{max} = cN_v \quad (2)$$

where c is a constant.

From Eq. (2), ΔE_{max} is proportional to the $\left|B_q^k\right|^2$. According to the values in Table 4, the sum of $\left|B_q^k\right|^2$ of Nd:LuAG is 14,087,040 cm^{-2} and larger than that of YAG (13,620,900 cm^{-2}), which is consistent with the experimental results, revealing that the Stark energy splitting of Nd:LuAG is larger than that of Nd:YAG.

The crystal field also can be illustrated by the chemical bond theory of complex structure crystals developed by Zhang [19,20], in which the chemical environmental parameter h related to the energy levels was introduced and can be expressed by the following equation:

$$h = [\sum_i \alpha_i f_c(i) Z(i)^2]^{1/2} \quad (3)$$

where α_i polarizability of the ligand bond volume in the type-i bond (in $Å^3$), $f_c(i)$ is covalency between central ion and chemical bond of ith ligand, $Z(i)$ stands for the presented charge of the ligands in the chemical bond of the type i. The covalency between central ions and ligands as well as the polarization effect from ligands are related to the effect of electron cloud swell, namely related to the crystal field interaction. The values of α_i, $f_c(i)$ and h in YAG and LuAG are listed in Table 5 [21], respectively. From Table 5, we can see that the polarization ratio, covalent and environmental parameters in LuAG are all more than that of YAG. The energy splitting is usually proportional to α_i, $f_c(i)$ and h.

3.3. Absorption and fluorescence spectra of Nd:LuAG polycrystalline powder

The room temperature absorption and fluorescence spectra of Nd:LuAG are shown in Fig. 5. The transitions of absorption and emission are assigned according to the reference [22]. In the absorption spectrum, the bands around 800 nm are assigned to $^4I_{9/2} \rightarrow {}^4F_{5/2}$ and $^2H_{9/2}$ transitions and the absorption intensity at 808 nm is the strongest. The FWHM of band at 808 nm is very broad and more than 6 nm, which is greater than that of Nd:YAG (<4 nm). Because laser diodes (LD) typically emit in a 5 nm wide spectral range and has a thermal shift of the peak wavelength, the broad band is very propitious to increase the pump efficiency and decrease the wavelength dependence of a pump LD on temperature. All bands correspond to the typical transitions from ground state $^4I_{9/2}$ to upper excited states, which are indicated in Fig. 5.

In the emission spectrum, there are three bands around 900, 1060 and 1350 nm. The bands at 900, 1060 and 1350 nm belong to the transitions from $^4F_{3/2}$ to $^4I_{9/2}$, $^4I_{11/2}$ and $^4I_{13/2}$, respectively. The transitions from $^4F_{3/2}$ to $^4I_{9/2}$ mainly include several peaks around 870, 884, 890, 896,899, 906, 941 and 947 nm, the transitions from $^4F_{3/2}$ to $^4I_{11/2}$ are composed of the peaks round 1053, 1064 and 1072 nm, the transitions from $^4F_{3/2}$ to $^4I_{13/2}$ mainly include the peaks at 1321, 1335,1339,1353, 1417, 1420, 1433 and 1443 nm. The fluorescence intensity at 1064 nm is much stronger than that at other wavelengths, and it is often served as the laser output wavelength.

Table 5
The values of the polarization ratio α_i, covalency $f_c(i)$ and the chemical environmental parameter h in YAG and LuAG.

Host	α_i	$f_c(i)$	h
YAG	0.370	0.066	0.884
LuAG	0.385	0.080	0.993

The fluorescence decay curve of $^4F_{3/2} \rightarrow {}^4I_{11/2}$ at room temperature is shown in Fig. 6. The decay curve can be fitted by the single exponential decay equation $I = I_0 e^{-t/\tau}$, and the fluorescence lifetime is determined to be 320 μs, which is longer than that of Nd:YAG (230 μs [23]). The longer lifetime is propitious to energy storage.

In addition, the emission cross section was also calculated by the following formula [24]

$$\sigma_{em}(\lambda) = \frac{\eta \lambda^5 I(\lambda)}{8\pi n^2 c \tau_f f_j \int \lambda I(\lambda) d\lambda} \quad (4)$$

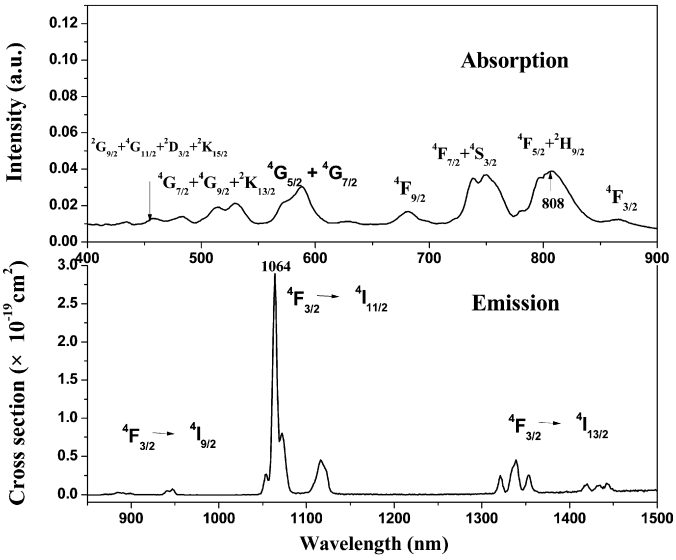

Fig. 5. The absorption and emission spectra of Nd:LuAG at room temperature.

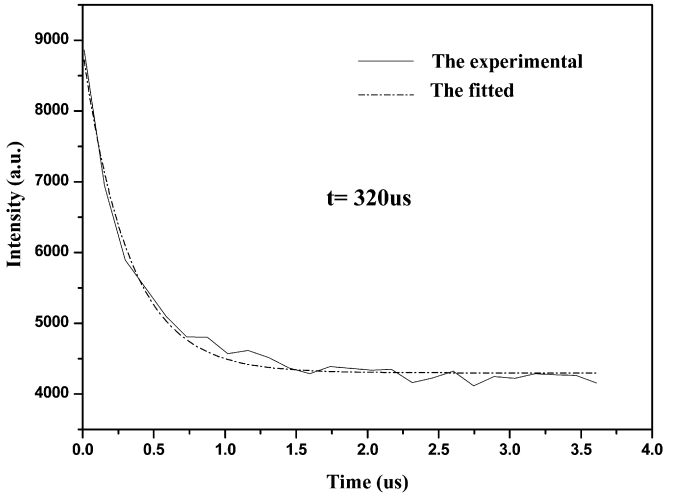

Fig. 6. The fitted decay time curve of Nd:LuAG under 1064 nm excitation.

$I(\lambda)$ is the intensity of corrected emission spectrum, τ_f is the fluorescence lifetime of the transition from excited manifold $^2F_{3/2}$ to $^4I_{11/2}$, c is the velocity of light, n is the refractive index, f_j is the fraction of the pumped population in state j given by the Boltzmann distribution, η is the radioactive quantum efficiency of the upper states. Here the Boltzmann distribution of the excited state is considered because of the small energy splitting of $^4F_{3/2}$ state, and the nonradioactive decay is negligible. The refractive index of Nd:LuAG is 1.83 [8]. The calculated emission cross section of Nd:LuAG at 1064 nm is 2.89×10^{-19} cm^2 and larger than that of Nd:YAG (2.8×10^{-19} cm^2 [25]). The large emission cross section is useful for laser operation.

4. Conclusions

The powder of Nd:$Lu_3Al_5O_{12}$ (Nd:LuAG) was synthesized by co-precipitation method. The DTA and XRD analyses show that Nd:LuAG polycrystalline phase can be formed above 900 °C and the particle sizes calcined at 900–1250 °C are in the range of 18–36 nm. The refined lattice constant and the cell volume are larger than pure LuAG. Compared with YAG, the crystal field interaction in Nd:LuAG is stronger. The room temperature absorption spectrum shows that Nd:LuAG has broad FWHM at 808 nm (more than 6 nm), which can increase the pumping efficiency and decrease the influence of temperature on the wavelength of pump laser diodes. The fluorescence lifetime and the emission cross section of the transition from $^4F_{3/2}$ to $^4I_{11/2}$ is 320 μs and 2.89×10^{-19} cm^2, respectively. Compared with Nd:YAG, the fluorescence lifetime is longer and the emission cross section is larger in Nd:LuAG, which is propitious for Nd:LuAG to apply in high energy lasers.

Acknowledgements

This work is supported by National Natural Science Fund of China (Grant no.50772112, 50872135) and Natural Science Fund of Anhui Province (No. 08040106820).

References

[1] M.R. Ali, S.M. Taher, Journal of Magnetism and Magnetic Materials 301 (2006) 433.
[2] Q.L. Zhang, S.T. Yin, A.H. Wang, J.Z. Xiao, Chinese Journal of Quantum Electronics 19 (2002) 481.
[3] M. Liu, S.W. Wang, D.Y. Tang, L.D. Chen, J. Ma, Journal of Rare Earth 27 (2009) 66.
[4] H. Zhou, X.H. Ma, G.T. Chen, W.C. Lv, Y. Wang, Z.Y. You, J.F. Li, Z.J. Zhu, C.Y. Tu, Journal of Alloys and Compounds 475 (2009) 555.
[5] C.R. Stanek, K.J. McClellan, M.R. Levy, C. Milanese, R.W. Grimes, Nuclear Instruments and Methods in Physics Research A 579 (2007) 27.
[6] H. Ogino, A. Yoshikawa, M. Nikl, J.A. Mares, J. Shimoyama, K. Kishio, Journal of Crystal Growth 311 (2009) 908.
[7] L.H. Gao, F.M. Gao, Materials Chemistry and Physics 113 (2009) 145.
[8] Y. Kuwano, K. Suda, N. Ishizawa, T. Yamada, Journal of Crystal Growth 260 (2004) 159.
[9] H. Ogino, A. Yoshikawa, M. Nikl, K. Kamada, T. Fukuda, Journal of Crystal Growth 287 (2006) 335.
[10] H. Ogino, A. Yoshikawa, J.H. Lee, M. Nikl, N. Solovieva, T. Fukuda, Journal of Crystal Growth 253 (2003) 314.
[11] Yu. Zorenko, B. Pavlyk, R. Turchak, T. Zorenko, V. Gorbenko, I. Konstankevych, V. Savchyn, T. Voznyak, Radiation Measurements 42 (2007) 557.
[12] A.A. Kaminskii, G.A. Bogomolova, Kh.S. Bagdasarov, A.G. Petrosyan, Optics Spectroscopy 39 (1975) 643.
[13] H.L. Li, X.J. Liu, L.P. Huang, Ceramic International 32 (2006) 309.
[14] Z.F. Wang, M. Xu, W.P. Zhang, M. Yin, Journal of Luminescence 122–123 (2007) 437.
[15] A.C. Larson, R.B. Von Dreele, General Structure Analysis System (GSAS), Los Alamos National Laboratory Report LAUR, 2004, pp. 86–748.
[16] Inorganic Crystal Structure Database of 73-1368.
[17] D.L. Sun, Q.L. Zhang, Z.B. Wang, J. Su, C.J. Gu, A.H. Wang, S.T. Yin, Materials Science and Engineering A 392 (2005) 278.
[18] E.A. Fidancev, C.K. Jayasankar, M.L. Blaise, P. Porcher, Journal of Physics C: Solid State Physics 19 (1986) 6451.
[19] S.Y. Zhang, Chemical Bond Theory of Complex Structure Crystals on Dielectric Description and Application, Science Press, Beijing, 2005.
[20] L. Li, S.H. Zhou, S.Y. Zhang, Solid state Sciences 10 (2008) 1173.
[21] S.Y. Zhang, Spectroscopy of Rare Earth Ions – Spectral Property and Spectral Theory, Science Press, Beijing, 2008.
[22] A.A. Kaminskii, Crystalline Lasers: Physical Processes and Operating Schemes, CRC Press, Boca Raton, 1996.
[23] W. Koechner, Solid-State Laser Engineering, Springer, Berlin, 2006.
[24] B.F. Aull, H.P. Jenssen, IEEE Journal of Quantum Electronics 18 (1982) 925.
[25] W.F. Krupke, M.D. Shinn, J.E. Marion, J.A. Caird, S.E. Stokowski, Journal of the Optics Society American B 3 (1986) 102.